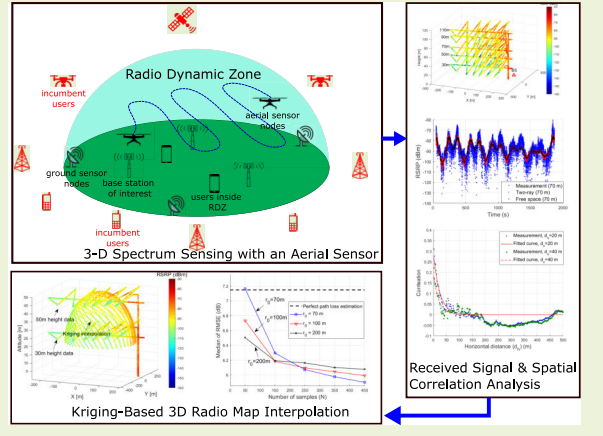


Kriging-Based 3-D Spectrum Awareness for Radio Dynamic Zones Using Aerial Spectrum Sensors

Sung Joon Maeng[®], *Member, IEEE*, Ozgur Ozdemir, *Member, IEEE*, İsmail Güvenç[®], *Fellow, IEEE*, and Mihail L. Sichitiu[®], *Member, IEEE*

Abstract—Radio dynamic zones (RDZs) are geographical areas within which dedicated spectrum resources are monitored and controlled to enable the development and testing of new spectrum technologies. Real-time spectrum awareness within an RDZ is critical for preventing interference with nearby incumbent users of the spectrum. In this article, we consider a 3-D RDZ scenario and propose to use unmanned aerial vehicles (UAVs) equipped with spectrum sensors to create and maintain a 3-D radio map of received signal power from different sources within the RDZ. In particular, we introduce a 3-D Kriging interpolation technique that uses realistic 3-D correlation models of the signal power extracted from extensive measurements carried out at the NSF Aerial Experimentation and Research Platform for Advanced Wireless (AERPAW) platform. Using C-band signal measurements by a UAV at altitudes between 30 and 110 m, we first develop realistic propagation models on air-



to-ground path loss, shadowing, spatial correlation, and semi-variogram, while taking into account the knowledge of antenna radiation patterns and ground reflection. Subsequently, we generate a 3-D radio map of a signal source within the RDZ using the Kriging interpolation and evaluate its sensitivity to the number of measurements used and their spatial distribution. Our results show that the proposed 3-D Kriging interpolation technique provides significantly better radio maps when compared with an approach that assumes perfect knowledge of path loss. Specifically, the root-mean-square error (RMSE) of the signal power prediction achieved by our proposed 3-D Kriging method is notably lower compared to that of the perfect path loss-based prediction, especially when the height difference between measured and the target locations is less than 20 m.

Index Terms—3-D spectrum awareness, Aerial Experimentation and Research Platform for Advanced Wireless (AER-PAW), antenna radiation pattern, I/Q samples, Kriging interpolation, long-term evolution (LTE), propagation modeling, radio dynamic zones (RDZ), reference signal received power (RSRP), Universal Software Radio Peripheral (USRP), unmanned aerial vehicle (UAV).

I. INTRODUCTION

A S THE demand for advanced wireless communication services continues to grow, efficient use of spectrum

Manuscript received 19 November 2023; revised 14 January 2024; accepted 15 January 2024. Date of publication 29 January 2024; date of current version 14 March 2024. This work was supported in part by the NSF Platforms for Advanced Wireless Research (PAWR) under Award CNS-1939334. The associate editor coordinating the review of this article and approving it for publication was Prof. Yongqiang Zhao. (Corresponding author: Sung Joon Maeng.)

Sung Joon Maeng is with the Department of Electrical and Electronic Engineering, Hanyang University, Ansan 15588, South Korea (e-mail: sjmaeng@hanyang.ac.kr).

Ozgur Ozdemir, İsmail Güvenç, and Mihail L. Sichitiu are with the Department of Electrical and Computer Engineering, North Carolina State University, Raleigh, NC 27606 USA (e-mail: oozdemi@ncsu.edu; iguvenc@ncsu.edu; mlsichit@ncsu.edu).

Digital Object Identifier 10.1109/JSEN.2024.3357430

resources is becoming increasingly vital for future wireless technologies. Therefore, the development, testing, and evaluation of effective mechanisms to improve spectrum efficiency and sharing have become imperative. Although there is a considerable body of literature that examines and analyzes spectrum sharing using theoretical models and simulations, there is a clear need to assess these approaches in real-world deployment scenarios, taking into account realistic propagation conditions.

In this particular context, the concept of radio dynamic zones (RDZs) emerges as a new concept [2], [3], [4], where geographical areas with dedicated spectrum resources are managed and controlled in real-time to test new wireless technologies. This management is achieved through the sensing of signals entering and leaving the zone [5]. RDZs serve

as testing grounds for novel spectrum sharing concepts and emerging technologies aimed at improving spectrum efficiency. In RDZs, it becomes crucial to ensure minimal or no interference to nearby incumbent users of the spectrum. Such receivers may include terrestrial receivers as well as aerial receivers, e.g., for coexistence with unmanned aerial vehicles (UAVs) and satellites. The use of radio environment maps (REMs) [6] presents an effective approach for constructing dynamic interference maps within an RDZ, which can be generated for each location and frequency of interest. REMs can be generated by collecting signal power data from deployed sensors and incorporating their corresponding location information [7]. However, it is often impractical to position sensors throughout the entire RDZ area. Instead, signal power at unknown locations can be predicted using signal processing techniques like Kriging [8], based on measurements from nearby sparsely deployed sensors and exploiting the spatial correlation of the signal.

In the existing literature, several studies have focused on modeling the spatial correlation of shadowing in received signals [9], [10], with experimental measurements provided in [11] and [12]. The application of Kriging for generating radio maps of signal power has been validated using both simulated and real datasets [13]. The potential of Kriging for spectrum monitoring and interference management has been explored in [14], while [15] extends Kriging interpolation to spectrum interpolation and analyzes it using measurement datasets. Spectrum occupancy monitoring of a 3-D volume area by using a UAV combined with path planning has been investigated in [16]. For ground-to-UAV communications in suburban environments, path loss and shadowing have been modeled based on measurement datasets [17], [18]. Additionally, the spatial correlation along the linear trajectory of a UAV has been investigated [19]. In our recent works, we introduce the RDZ concept and discuss its features and requirements [3]. Furthermore, we propose an out-of-zone signal leakage sensing algorithm using Kriging in the 2-D plane of the RDZ [20]. Notably, to the best of our knowledge, the literature does not address the use of Kriging to obtain a 3-D aerial radio map based on measurements obtained from UAVs.

In this article, we propose to develop and use a 3-D radio map to effectively sense signal leakage from an RDZ to the receivers outside of the RDZ. We employ a UAV as a mobile aerial sensor, collecting signal power measurements from distinct receivers within the RDZ. The 3-D interpolation of the collected signal power is performed using the Kriging technique. The proposed method is thoroughly analyzed and validated through a measurement campaign. The main contributions of this article can be summarized as follows.

1) Modeling 3-D radio propagation: Considering a 3-D spectrum sensing scenario, we develop and analyze a path loss model that accounts for spatially correlated shadowing, two-ray wireless propagation, and measured antenna radiation patterns to accurately model 3-D radio propagation. We integrate 3-D antenna measurements obtained in an anechoic chamber and study improvements in model accuracy when compared to using dipole and omnidirectional antenna patterns.

2) Comparison with measurement data: We evaluate and compare the accuracy of our proposed 3-D propagation models with the measurement data collected using software-defined radios (SDRs) at various UAV altitudes. This analysis provides valuable insights into the performance and reliability of the proposed approach. We show through simulations using real measurement datasets that the root-mean-square error (RMSE) of the signal power prediction achieved by our proposed 3-D Kriging method is notably lower compared to that of the perfect path loss-based prediction, especially when the height difference between measured and the target locations is less than 20 m.

The rest of this article is organized as follows. In Section II, we present the system model for 3-D spectrum sensing, radio propagation, and spatial correlation in an RDZ, while in Section III, we introduce the Kriging-based signal interpolation method for generating a 3-D radio map. In Section IV, we describe the details of our measurement campaigns for obtaining I/Q signal samples at a UAV from a long-term evolution (LTE)-based signal source on the ground, and our measurements in an anechoic chamber for characterizing the antenna radiation patterns. In Section V, we analyze the effectiveness of the proposed 3-D path-loss models in predicting the received signal power at different UAV altitudes and locations. We present numerical results on Kriging-based 3-D radio map interpolation in Section VI and the last section concludes this article.

II. SYSTEM MODEL

In this section, we present the models utilized for spectrum sensing within an RDZ. Specifically, we consider a scenario where an aerial spectrum sensor captures received signals from a base station (BS). Radio propagation, correlation, and antenna radiation pattern models are also presented.

A. 3-D Spectrum Sensing With an Aerial Mobile Sensor

An RDZ should protect incumbent users outside of the zone by controlling and managing interference signals radiating from inside the zone. The incumbent users may include smart devices and aerial vehicles, as well as sensitive scientific passive receivers such as satellites and ground-based radio astronomy receivers in radio quiet zones (RQZs) [21]. Our envisioned RDZ concept is illustrated in Fig. 1. The real-time spectrum sensing within the boundary of the RDZs is conducted by deployed fixed/mobile ground and aerial sensor nodes, which is an essential technique to manage dynamic spectrum usage. The UAV moves across the RDZ space along a multialtitude trajectory, capturing signal data throughout.

This article primarily focuses on the study of real-time signal sensing in the volume of space to monitor the signal leakage from RDZs. Mobile aerial nodes, in the form of UAVs, collect signal power data as they follow predefined trajectories. Subsequently, the RDZ system leverages the collected dataset from the aerial nodes to generate a radio map depicting the signal power surrounding the RDZ space. The interpolation of this dataset facilitates the construction of a comprehensive representation of signal power distribution.

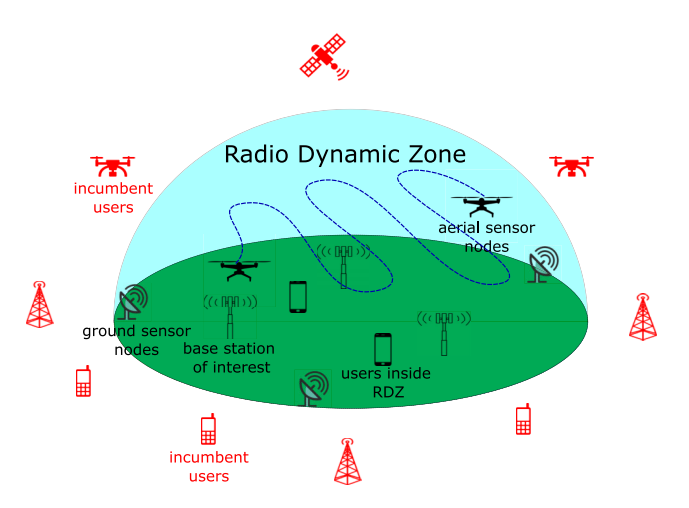


Fig. 1. Illustration of an RDZ with aerial and ground sensors and users.

In particular, we investigate a single BS and a single aerial sensor scenario by using an experimental dataset collected by a UAV. The significance of using UAVs for obtaining 3-D spectrum measurements is noteworthy since any spectrum measurements collected exclusively from the ground will not be able to characterize spectrum occupancy at higher altitudes due to complex propagation conditions in 3-D space.

B. Radio Propagation Model

The location of a BS and a UAV can be represented by

$$\mathbf{l}^{bs} = (\psi^{bs}, \omega^{bs}, h^{bs}), \quad \mathbf{l}^{uav}(t) = (\psi^{uav}, \omega^{uav}, h^{uav}) \quad (1)$$

where ψ , ω , and h denote the latitude, longitude, and altitude of the location. Although the location can be generally represented by x, y, z in 3-D Cartesian coordinates, we express it by latitude, longitude, and altitude to use the information given by GPS sensors. The time-varying location of a UAV is given by $\mathbf{l}^{\text{uav}}(t)$. The horizontal distance and the vertical distance between a BS and a UAV can be expressed as [22]

$$\textit{d}_{h}(\mathbf{l}^{bs}, \mathbf{l}^{uav}) = \arccos \left(\sin \psi^{uav} \sin \psi^{bs} + \cos \psi^{uav} \cos \psi^{bs} \right.$$

$$\times \cos(\omega^{\rm bs} - \omega^{\rm uav}) \times A$$
 (2)

$$d_{\mathbf{v}}(\mathbf{l}^{\mathrm{bs}}, \mathbf{l}^{\mathrm{uav}}) = |h^{\mathrm{bs}} - h^{\mathrm{uav}}| \tag{3}$$

where A is the radius of the earth (\approx 6 378 137 m). Then, the 3-D distance between a BS and a UAV is given by

$$d_{3-D}(\mathbf{l}^{\text{bs}}, \mathbf{l}^{\text{uav}}) = \sqrt{d_{\text{h}}(l^{\text{bs}}, l^{\text{uav}})^2 + d_{\text{v}}(l^{\text{bs}}, l^{\text{uav}})^2}.$$
 (4)

Next, the elevation angle between a BS and a UAV is

$$\theta_l = \tan^{-1} \left(d_{\rm v} / d_{\rm h} \right). \tag{5}$$

To develop a propagation model, we make use of a first-order approximation and consider the rural environment in which we collect measurements. In this scenario, we employ the two-ray ground reflection model to represent the path loss between a BS and a UAV. This model accounts for a line-of-sight (LoS) path as well as a strong ground reflection path, both contributing to the received signal as the two dominant paths in an open area such as a rural environment. The path

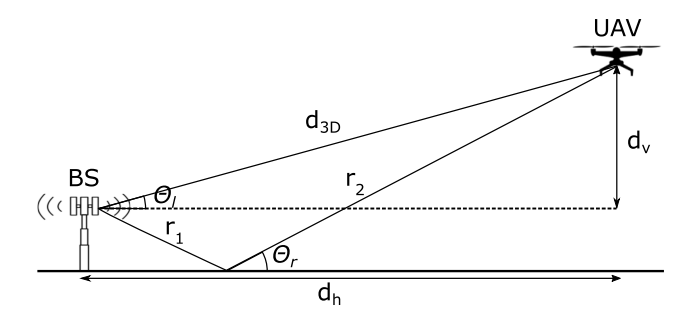


Fig. 2. Illustration of the two-ray ground reflection model.

loss characterized by the two-ray ground reflection model can be expressed as follows [23, Ch. 2]:

$$\begin{aligned}
& = \left(\frac{\lambda}{4\pi}\right)^{2} \left| \frac{\sqrt{\mathsf{G}_{bs}(\phi_{l}, \theta_{l})\mathsf{G}_{uav}(\phi_{l}, \theta_{l})}}{\frac{d_{3-D}}{\mathsf{LoS \, signal}}} \right| \\
& + \underbrace{\frac{\Gamma(\theta_{r})\sqrt{\mathsf{G}_{bs}(\phi_{r}, \theta_{r})\mathsf{G}_{uav}(\phi_{r}, \theta_{r})} e^{-j\Delta\tau}}{r_{1} + r_{2}}}_{\mathsf{ground \, reflected \, signal}} \right|^{2} \tag{6}$$

where $G_{bs}(\phi,\theta)$, $G_{uav}(\phi,\theta)$, λ , and ϕ denote the antenna gain of a BS, antenna gain of a UAV, wavelength, and azimuth angle, respectively, $\theta_r = \tan^{-1}((h^{bs} + h^{uav})/d_h)$ represents ground reflection angle, and $\Delta \tau = ((2\pi(r_1 + r_2 - d_{3-D}))/\lambda)$ indicates the phase difference between two paths. The distance and the angle parameters in the two-ray ground reflection model are illustrated in Fig. 2. The ground reflection coefficient with the vertically polarized signal is given by

$$\Gamma(\theta_r) = \frac{\varepsilon_0 \sin \theta_r - \sqrt{\varepsilon_0 - \cos^2 \theta_r}}{\varepsilon_0 \sin \theta_r + \sqrt{\varepsilon_0 - \cos^2 \theta_r}}$$
(7)

where ε_0 is the relative permittivity of the ground and the value depends on the type of the ground. Two signal components in (6) are received and combined with a phase difference. If we only consider the first LoS term in the path loss, we can obtain the free-space path loss model, given as

$$\mathsf{PL}_{\mathsf{fs}} = \left(\frac{\lambda}{4\pi}\right)^2 \left| \frac{\sqrt{\mathsf{G}_{\mathsf{bs}}(\theta_l)\mathsf{G}_{\mathsf{uav}}(\theta_l)}}{d_{\mathsf{3-D}}} \right|^2. \tag{8}$$

Using (6), the received signal power of a UAV in dB scale can be expressed as

$$r = \mathsf{P}_{\mathsf{Tx}} - \mathsf{PL}_{\mathsf{twm}}^{(\mathsf{dB})} + w \tag{9}$$

where P_{Tx} and w denote transmit power and shadowing component, respectively. The path loss term in (9) is converted to dB scale. The shadowing term generally follows a lognormal distribution and is modeled by a zero-mean Gaussian process with a spatial covariance [9]. The correlation between received signals at two different locations is generally characterized by the function of the distance between those locations. We do not take into account small-scale fading in the received signal

since we assume that the effect is eliminated by averaging the samples within the proper time interval [11].

C. Spatial Correlation Model of Received Signal

In this section, we focus on describing the correlation function between the received signals at different locations of a UAV. Since the spatial correlation primarily depends on the shadowing component (w) in the received signal in (9), we can capture the correlation between received signals (r)using the correlation between the shadowing components without loss of generality. It is well-known that the correlation between two different locations is characterized by a function of their physical distance. Typically, this correlation exponentially attenuates as the physical distance between the locations increases [11]. However, most existing works in the literature primarily focus on terrestrial networks and do not fully consider 3-D topologies. Due to this limitation, the spatial correlation between two locations with different vertical positions (heights) has not been extensively studied to our best knowledge. Considering the unique characteristics of UAVbased scenarios, where altitude plays a crucial role, it becomes essential to investigate and understand the spatial correlation between locations at different vertical positions.

We first model the spatial correlation as a function of the vertical distance $(d_{\rm v})$ and the horizontal distance $(d_{\rm h})$. Then, we define the correlation function between 3-D locations as a function of both the vertical distance and the horizontal distance. The spatial correlation between two different locations of a UAV, i.e., between $l_i^{\rm uav}$ and $l_j^{\rm uav}$, can be expressed as

$$R(l_i^{\text{uav}}, l_j^{\text{uav}}) = R(d_v, d_h) = \frac{\mathbb{E}\left[w(l_i^{\text{uav}})w(l_j^{\text{uav}})\right]}{\sigma_w^2}$$
(10)

where σ_w^2 is the variance of shadowing. Once again, the proposed correlation is the function of both the vertical distance and the horizontal distance.

D. Antenna Radiation Model

The antenna gain effect of a transmitter and a receiver in the received signal is captured in the path loss model in (6), using $G_{bs}(\phi,\theta)$ and $G_{uav}(\phi,\theta)$. In typical terrestrial communications, the antenna gain is simply modeled by a constant gain. This is due to the fact that a dipole antenna is usually characterized as an omnidirectional antenna radiation pattern in the azimuth angle domain, or sectored directional antennas make the antenna pattern mostly uniform in the azimuth angle domain. However, air-to-ground communications require considering the variation of the antenna gain in the elevation angle domain, which is typically far from being uniform. Therefore, we should consider the elevation angle-dependent radiation pattern in modeling the antenna gain.

It is worthwhile to note that modeling of the 3-D antenna radiation pattern and the spatial correlation in the 3-D air-to-ground channel is necessary to design the Kriging-based 3-D radio map interpolation. Specifically, the received signal power of a UAV consists of the transmit power, the path loss, and the shadowing component in (9). To extract the

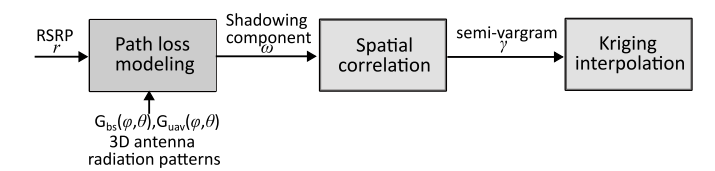


Fig. 3. Block diagram of a procedure to apply Kriging interpolation from the measured RSRP.

shadowing component from the received signal and calculate the spatial correlation in (10), we need to know the path loss term considering the 3-D antenna radiation pattern. In the end, the semi-variogram is obtained using the spatial correlation, which is subsequently used in the Kriging interpolation. The detailed approach to obtaining the semi-variogram from the spatial correlation and utilizing it in Kriging interpolation is described in Section III below.

III. 3-D RADIO MAP INTERPOLATION USING KRIGING

In this section, we introduce an efficient radio map interpolation technique using Kriging [14]. This method utilizes measurement data obtained from sparsely deployed spectrum sensors within an RDZ, and allows us to estimate signal values at unsampled locations based on the available measurements. We first introduce how to calculate a semi-variogram, and subsequently, introduce our Kriging-based interpolation approach for 3-D RDZ scenarios. Different than the existing Kriging techniques in the literature, we consider the 3-D geometry in spatial correlation with a portable aerial sensor, which enables us to interpolate the radio map in a 3-D volume.

As seen in Fig. 3, to implement Kriging interpolation, we need to calculate the path loss and the spatial correlation. We will study how to apply the proposed Kriging-based 3-D interpolation in Section III, and we describe our measurement campaign to collect the real dataset in Section IV, and then in Section V, we analyze the measurement dataset based on the radio propagation model and the 3-D antenna pattern. At the end, in Section VI, we evaluate the proposed interpolation technique based on the real datasets.

A. Semi-Variogram

In geostatistics, the semi-variogram represents the degree of spatial dependency on different locations which is utilized in Kriging interpolation. The semi-variogram between a UAV's locations l_i^{uav} , l_i^{vav} is defined as

$$\gamma\left(l_{i}^{\mathrm{uav}}, l_{j}^{\mathrm{uav}}\right) = \frac{1}{2} \mathrm{var}\left(r\left(l_{i}^{\mathrm{uav}}\right) - r\left(l_{j}^{\mathrm{uav}}\right)\right). \tag{11}$$

If the covariance function of a stationary process exists, we can obtain the semi-variogram from the spatial correlation in (10) as follows for our considered 3-D RDZ scenario [24]:

$$\begin{aligned}
\nu(l_i^{\text{uav}}, l_j^{\text{uav}}) \\
&= \frac{\sigma_w^2}{2} \left(R(l_i^{\text{uav}}, l_i^{\text{uav}}) + R(l_j^{\text{uav}}, l_j^{\text{uav}}) - 2R(l_i^{\text{uav}}, l_j^{\text{uav}}) \right) \\
&= \sigma_w^2 \left(1 - R(l_i^{\text{uav}}, l_j^{\text{uav}}) \right) = \sigma_w^2 \left(1 - R(d_v, d_h) \right)
\end{aligned} \tag{12}$$

where σ_w^2 is the variance of the shadowing term w in (9) as defined earlier, and $R(l_i^{\text{uav}}, l_i^{\text{uav}})$ is as in (10). We assume σ_w^2 is constant at a given set of locations while deriving (12).

B. Kriging Interpolation

The ordinary Kriging is the optimal prediction method in squared-error loss from the observed data at known spatial locations where the error of the spatial prediction of an unknown location is minimized [24]. It interpolates the signal strength of the arbitrary locations by using the linear combination of the signal strength of the nearby locations. The ordinary Kriging problem can be formulated as follows [14]:

$$\min_{\mu_1, \dots, \mu_M} \mathbb{E}\left[\left(\hat{r} \left(\mathbf{l}_0^{\text{uav}} \right) - r \left(\mathbf{l}_0^{\text{uav}} \right) \right)^2 \right]$$
 (13)

s.t.
$$\hat{r}(\mathbf{l}_0^{\text{uav}}) = \sum_{i=1}^{M} \mu_i r(\mathbf{l}_i^{\text{uav}})$$
 (14a)

$$\sum_{i=1}^{M} \mu_i = 1 \tag{14b}$$

where l_0^{uav} is a location to predict an unknown parameter, μ_i $(i=1,\ldots,M)$ are weighting parameters, and M indicates the number of nearby measured samples to use.

The above problem can be solved by following steps [14]. First, we convert the original problem to an equivalent Lagrange expression

$$\min_{\mu_1,\dots,\mu_M} \mathbb{E}\left[\left(r(l_0^{\text{uav}}) - \sum_{i=1}^M \mu_i r(l_i^{\text{uav}})\right)^2\right] - \kappa \left(\sum_{i=1}^M \mu_i - 1\right)$$
(15)

where κ denotes the Lagrange multiplier. After a few steps, the objective function in (15) can be reformulated as

$$\sigma_w^2 + 2\sum_{i=1}^M \mu_i \gamma \left(l_0^{\text{uav}}, l_i^{\text{uav}} \right) - \sum_{i=1}^M \sum_{j=1}^M \mu_i \mu_j \gamma \left(l_i^{\text{uav}}, l_j^{\text{uav}} \right) - \kappa \left(\sum_{i=1}^M \mu_i - 1 \right)$$
(16)

where $\gamma(l_i^{\text{uav}}, l_j^{\text{uav}})$ is as defined in (11). Finally, we can find the optimal solution by the finding first derivative of (16) with respect to μ_1, \ldots, μ_M , which is given by

$$\sum_{i=1}^{M} \mu_j \gamma \left(l_i^{\text{uav}}, l_j^{\text{uav}} \right) - \gamma \left(l_0^{\text{uav}}, l_i^{\text{uav}} \right) + \kappa' = 0.$$
 (17)

We can also express (17) as a linear matrix equation as

$$\begin{bmatrix} \gamma\left(l_{1}^{\text{uav}}, l_{1}^{\text{uav}}\right) & \cdots & \gamma\left(l_{1}^{\text{uav}}, l_{M}^{\text{uav}}\right) & 1 \\ \gamma\left(l_{2}^{\text{uav}}, l_{1}^{\text{uav}}\right) & \cdots & \gamma\left(l_{2}^{\text{uav}}, l_{M}^{\text{uav}}\right) & 1 \\ \vdots & \vdots & \vdots & \vdots & \vdots \\ \gamma\left(l_{M}^{\text{uav}}, l_{1}^{\text{uav}}\right) & \cdots & \gamma\left(l_{M}^{\text{uav}}, l_{M}^{\text{uav}}\right) & 1 \\ 1 & \cdots & 1 & 0 \end{bmatrix} \begin{bmatrix} \mu_{1} \\ \mu_{2} \\ \vdots \\ \mu_{M} \\ \kappa' \end{bmatrix}$$

$$= \begin{bmatrix} \gamma \left(l_0^{\text{uav}}, l_1^{\text{uav}} \right) \\ \gamma \left(l_0^{\text{uav}}, l_2^{\text{uav}} \right) \\ \vdots \\ \gamma \left(l_0^{\text{uav}}, l_M^{\text{uav}} \right) \\ 1 \end{bmatrix}. \quad (18)$$

Then, we can obtain the optimal μ_1^*, \dots, μ_M^* from (18) and interpolate the received powers at unknown location l_0^{uav} by

$$\hat{r}(l_0^{\text{uav}}) = \sum_{i=1}^{M} \mu_i^{\star} r(l_i^{\text{uav}}). \tag{19}$$

Note that accurate characterization of the 3-D semi-variogram in (11) is critical for the interpolation in (19). Section IV describes our measurements that will be used to characterize the 3-D semi-variogram.

IV. MEASUREMENT CAMPAIGN OVERVIEW

In this section, we describe the details of our radio propagation measurements. We present our measurement setup, define UAV trajectory used, and describe our approach for characterizing antenna effects.

A. Measurement Setup

The measurement campaign was conducted at the Lake Wheeler Road Field Laboratory (LWRFL) site in Raleigh, NC, USA, which is one of the two sites in the NSF Aerial Experimentation and Research Platform for Advanced Wireless (AERPAW). The experimental area, depicted in Fig. 4(a), can be classified as an open rural environment, ensuring LoS conditions between a UAV and the BS throughout the entire duration of the experiments. Fig. 4(b) and (c) presents photos of the BS tower and the drone used during the measurement campaign. The BS tower stands at a height of 10 m and is equipped with a single dipole transmit antenna. On the other hand, the drone is equipped with a vertically oriented single dipole receiver antenna and a GPS receiver to accurately track its position. To facilitate the measurements, the srsRAN open-source SDR software was utilized to implement an LTE evolved NodeB (eNB) at the BS tower, as shown in Fig. 4(b). The eNB continuously transmitted common reference symbols (CRSs) during the measurement campaign.

During the measurement campaign, the drone collects raw I/Q data samples using an SDR that is attached to it. Specifically, the Universal Software Radio Peripheral (USRP) B205mini from National Instruments (NI) is utilized as the SDR device, both at the BS tower and on the UAV. For post-processing the raw I/Q data, we employ MATLAB's LTE toolbox. Within this toolbox, we calculate the reference signal received power (RSRP) for each location of the UAV. To ensure efficient processing and analysis, we collect 20 ms segments of data out of every 100 ms. Within each 20 ms segment, we extract a 10-ms duration for subsequent post-processing. Throughout this article, the terms "received signal" and "RSRP" are used interchangeably to refer to the measured signal strength. The major specifications of the transmitter and the receiver are listed in Table I.





(b) BS tower



Fig. 4. (a) Area where air-to-ground propagation data has been collected in AERPAW. (b) Fixed node tower (30 feet high) that includes the SDR serving as the LTE eNB. (c) Drone that carries the receiver SDR

TABLE I
MEASUREMENT SETUP FOR EXPERIMENTS

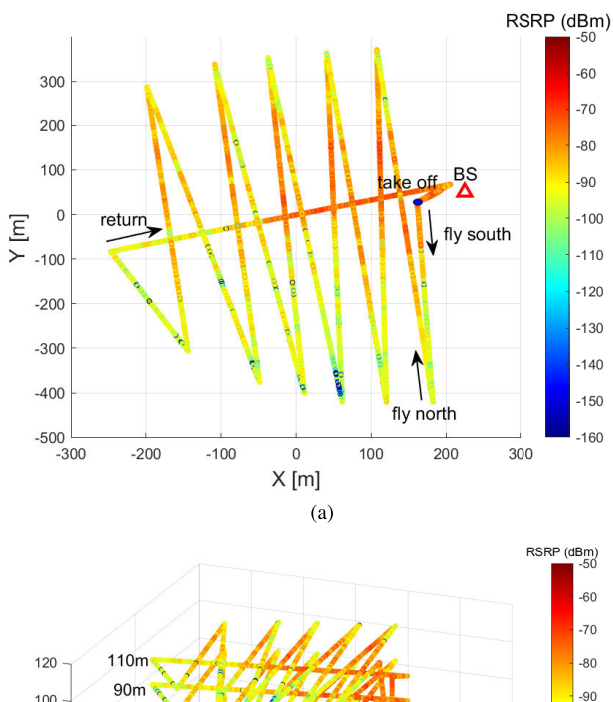
| BS Tower (Transmitter) | | |
|------------------------|-------------------------------|--|
| Technology | LTE | |
| Tower height | 10 m | |
| Transmit power | 10 dBm | |
| Carrier frequency | 3.51 GHz | |
| Bandwidth | 1.4 MHz | |
| Antenna | Dipole antenna (RM-WB1) | |
| UAV (Receiver) | | |
| Antenna | Dipole antenna (SA-1400-5900) | |
| UAV heights | {30, 50, 70, 90, 110} m | |

B. UAV Trajectory

We conduct the experiments multiple times by changing the altitude (height) of the UAV from 30 to 110 m at increments of 20 m. In each flight, the UAV flies an identical predefined trajectory with a different fixed height. In particular, the UAV flies on a zig-zag pattern through the experiment site, between south and north waypoints, and it eventually flies back to the starting point. The top view (at h=110 m) and the 3-D view of the UAV trajectories along with measured RSRPs are illustrated in Fig. 5 for flight trajectories at 30, 50, 70, 90, and 110 m.

C. Antenna Radiation Pattern Characterization

The dipole antenna used in our experiments generally exhibits omnidirectional radiation patterns in the azimuth angle domain, but oval-shaped radiation patterns in the



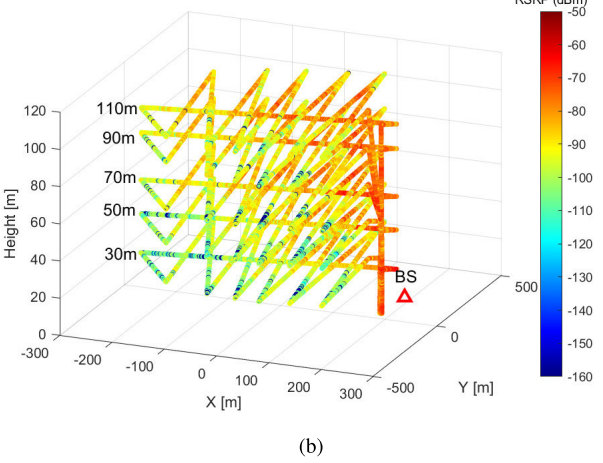
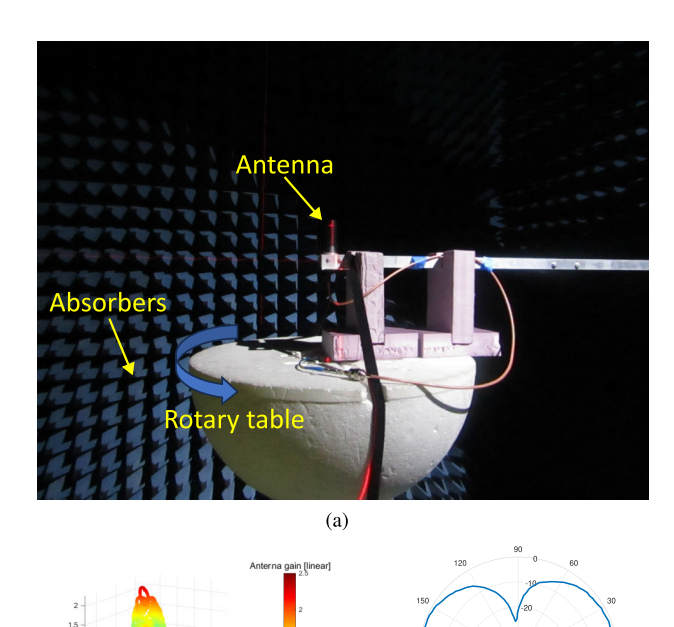


Fig. 5. Trajectory of the UAV and measured RSRP in RDZ experiments. Multiple flights with different heights are plotted in the bottom figure. (a) Top view of trajectory and RSRPs ($h=110\,\text{m}$). (b) 3-D view of trajectory and RSRP.

elevation angle domain. The radiation pattern also varies with the carrier frequency. We obtained the antenna pattern specifications for the Rx dipole antenna (SA-1400-5900) from the vendor's specification sheet, and it shows a typical donut-shaped dipole pattern that remains consistent across different carrier frequencies [25]. Specifically, in the specification sheet, the antenna patterns for 1.4, 1.7, 2.4, 4.4, and 5.8 GHz frequencies are provided and all of them have similar dipole patterns. Therefore, we adopted the 2.4-GHz frequency antenna pattern from the specification sheet for our analysis. However, the Tx dipole antenna (RM-WB1-DN) exhibited different elevation angle domain patterns depending on the carrier frequency and had an asymmetric pattern that did not guarantee omnidirectionality in the azimuth angle domain [26]. Furthermore, the specification sheet did not provide the radiation pattern for the specific carrier frequency (3.51 GHz) used in our experiments. To obtain the exact antenna radiation pattern for the 3.51 GHz frequency, we conducted separate measurements of the 3-D antenna pattern using an anechoic chamber facility located at Wireless Research Center (WRC), Wake Forest, NC, USA.



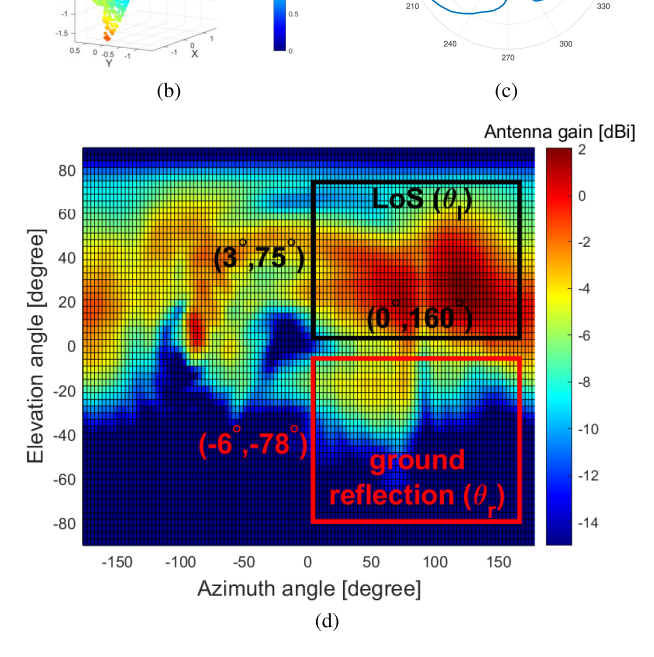


Fig. 6. Anechoic chamber setup for the 3-D antenna pattern measurement and the Tx, Rx, and combined antenna patterns we used for the analysis. (a) Anechoic chamber setup for Tx antenna pattern measurement. The center point of the chamber is adjusted to the tip of the antenna by the crossed laser lines. (b) Measured Tx antenna pattern in Cartesian coordinates at 3.5 GHz (by the gain in linear scale). (c) Rx antenna pattern for the elevation angle domain at 2.4 GHz (gain in dB scale from the specification sheet). (d) Combined (Tx + Rx) antenna pattern in 2-D angle domain in dB scale. Only the angle space in the black rectangle is used for LoS between the BS tower and the UAV in the experiment (θ_1), and the red rectangle is used for the ground reflection angles (θ_T).

Fig. 6(a) shows a photo of the setup in the anechoic chamber during the measurement of the Tx antenna's 3-D pattern. Fig. 6(b) displays the output of the antenna measurement, visualizing the antenna pattern in 3-D Cartesian coordinates. It can be observed that the antenna pattern is not purely omnidirectional in the azimuth angle domain, and the directivity in

the elevation angle domain is not straightforward. In contrast, Fig. 6(c) shows the elevation angle domain antenna pattern of the Rx antenna as provided in the specification sheet, where the antenna pattern is specified as omnidirectional with uniform gain in the azimuth domain. Fig. 6(d) illustrates the combined antenna gain from the Tx and Rx antenna patterns from Fig. 6(b) and (c), respectively, represented in the azimuth and elevation angle domain. For all UAV heights in our experiments, the LoS angles between the Tx tower and the UAV were within the angle space covered by the black rectangular area, while the ground reflection angles between Tx tower and the UAV were covered by the red rectangular area, which are illustrated in Fig. 2. This implies that the antenna pattern used for the analysis is limited to the angles within this space.

V. AIR-TO-GROUND PROPAGATION MODELING AND ANALYSIS

In this section, we review how we post-process the data for correcting errors in altitude reported by the UAV's GPS. Subsequently, we model the measured RSRP using different 3-D propagation models that take into account two-ray multipath model and 3-D antenna pattern.

A. Post-Measurement Correction of Altitude and RSRP

During the measurements, we encountered calibration errors caused by limitations in the SDR hardware. Specifically, the USRP mounted on the UAV exhibited a power level calibration error, resulting in a constant offset power throughout the experiment. To address this issue, we conducted a separate experiment to measure and determine the offset at the USRP, which was found to be 98 dB. Subsequently, we added this offset to the calculated RSRP values obtained from subsequent experiments, effectively compensating for the calibration offset.

Additionally, the GPS receiver carried by the UAV exhibited an altitude mismatch. We observed an altitude drift of approximately 6 m after the UAV landed, when compared with the initial altitude of the UAV. To rectify this mismatch, we applied a linear compensation approach (see [27, Fig. 6]). This involved adjusting the altitude measurements such that the altitude at the end of the flight matched the altitude of the initial measurement. By applying this compensation, we aimed to ensure accurate altitude data throughout the experiment.

B. Antenna Radiation Pattern Effect in Path Loss Analysis

In this section, we analyze the effect of antenna radiation patterns on the path loss fitting to the RSRP from the experiments. We consider three different antenna pattern setups for comparison: 1) Tx and Rx 3-D antenna patterns described in Section IV-C and Fig. 6; 2) the donut shape dipole antenna pattern using the formulation for both Tx and Rx antennas; and 3) constant azimuth and elevation antenna gain for both Tx and Rx antennas. The dipole antenna pattern formula in

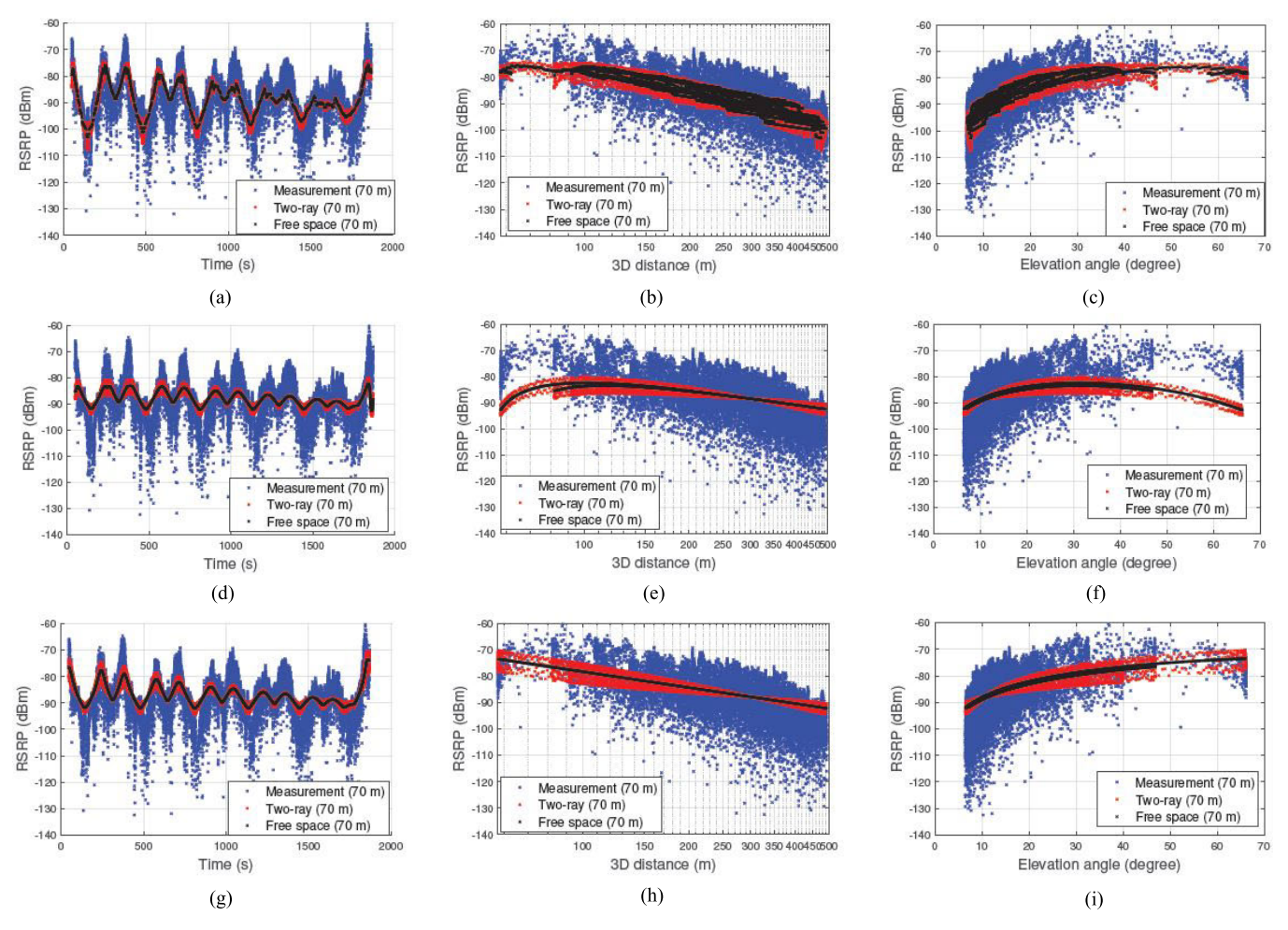


Fig. 7. RSRP fitting with different path loss models and antenna patterns in time, distance, and elevation angle domains. (a) RSRP versus time (measured antenna pattern). (b) RSRP versus 3-D distance (measured antenna pattern). (c) RSRP versus elevation angle (measured antenna pattern). (d) RSRP versus time (dipole antenna pattern). (e) RSRP versus 3-D distance (dipole antenna pattern). (f) RSRP versus elevation angle (dipole antenna pattern). (g) RSRP versus time (omnidirectional antenna pattern). (h) RSRP versus 3-D distance (omnidirectional antenna pattern). (i) RSRP versus elevation angle (omnidirectional antenna pattern).

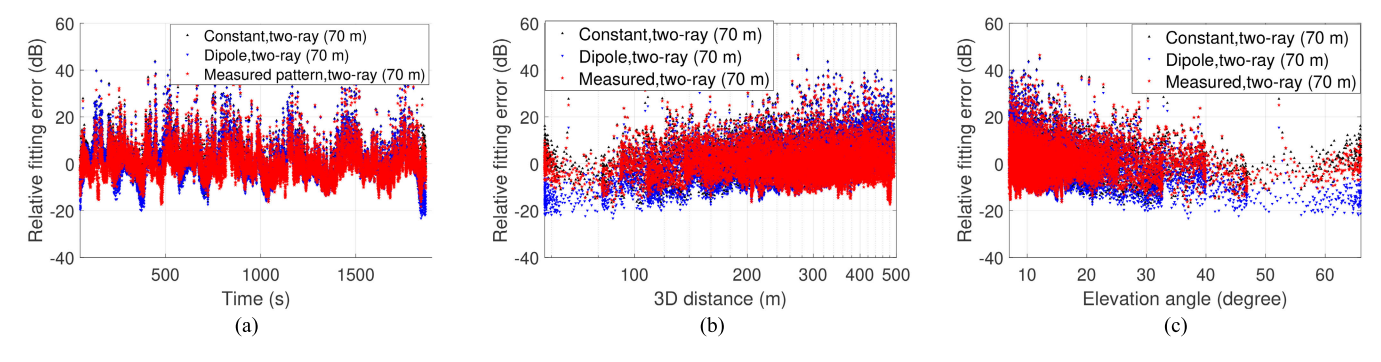


Fig. 8. Relative fitting error between measured RSRP and the two-ray path loss model with different antenna patterns in time, distance, and elevation angle domains. (a) Fitting error versus time. (b) Fitting error versus 3-D distance. (c) Fitting error versus elevation angle.

the second case is given by [28]

$$G_{bs}(\theta) = G_{uav}(\theta) = \frac{\cos\left(\frac{\pi}{2}\cos\theta\right)}{\sin\theta}.$$
 (20)

Figs. 7–9 provide a comprehensive analysis of the RSRP fitting results using different antenna patterns and path loss models in (6) and (8). In Fig. 7, the RSRP curves for a UAV height of 70 m are presented, along with the fitting

results obtained from the free space and two-ray path loss models with different antenna patterns. It is observed that the antenna pattern described in Section IV-C provides the best fit to the RSRP curves, while the dipole pattern in (20) results in the worst fit. Additionally, Fig. 7(a) highlights that the two-ray path loss model performs better than the free-space path loss model in capturing the deep fading of RSRP.

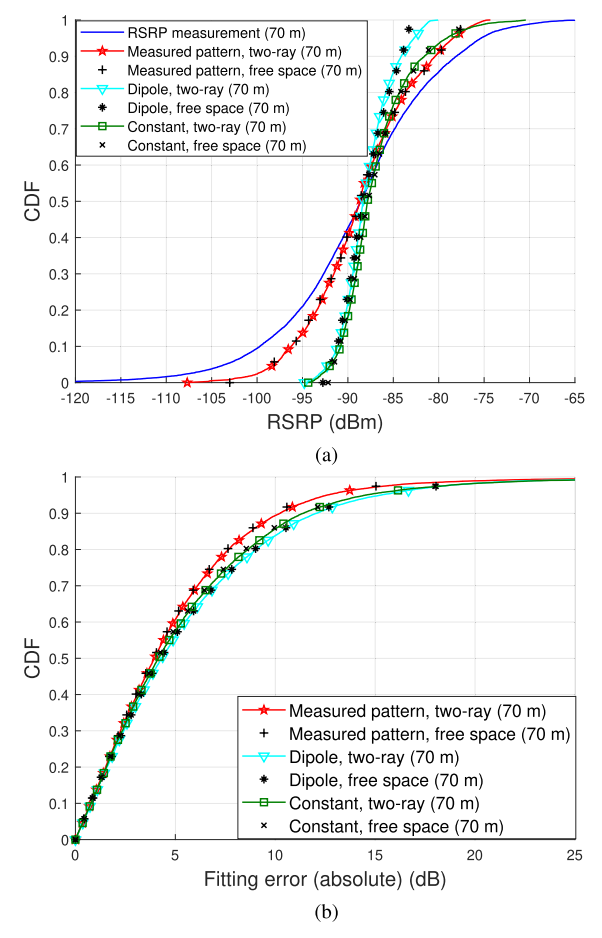


Fig. 9. CDF of RSRP and the fitting error with path loss models by different antenna radiation patterns. The measured antenna pattern in Fig. 6 achieves the closest fitting to the RSRP measurements. (a) cdf of RSRP. (b) cdf of fitting error between measured RSRP and path loss models.

Fig. 8 also evaluates the fitting error with different antenna patterns in time, distance, and elevation domains. It is observed that the dipole antenna pattern has the largest fitting error in short and long distances. We also observe that the fitting error is relatively high in small elevation angles. It implies that the effect of scattering from the objects around the test site increases the variance of the error when the elevation angle is low. Overall, these results demonstrate that the choice of antenna pattern and path loss model significantly impacts the accuracy of RSRP fitting for air-to-ground communication links. The 3-D antenna radiation pattern described in Section IV-C, combined with the two-ray path loss model, provides the best fit to the measured RSRP and minimizes the fitting error.

To further evaluate the performance, Fig. 9 presents the cumulative distribution function (cdf) of the RSRP for the 70-m height measurement, along with the fitting results obtained from the path loss models and different antenna patterns. The cdf of the two-ray path loss model with the antenna pattern in Section IV-C matches closest with the cdf of the measured RSRP, indicating a better fit. Fig. 9(b) shows the fitting error, which is calculated by subtracting the measured RSRP from the fit RSRP using the path loss models. It is observed that the fitting error is the smallest when using the two-ray path loss model with the antenna pattern in Section IV-C.

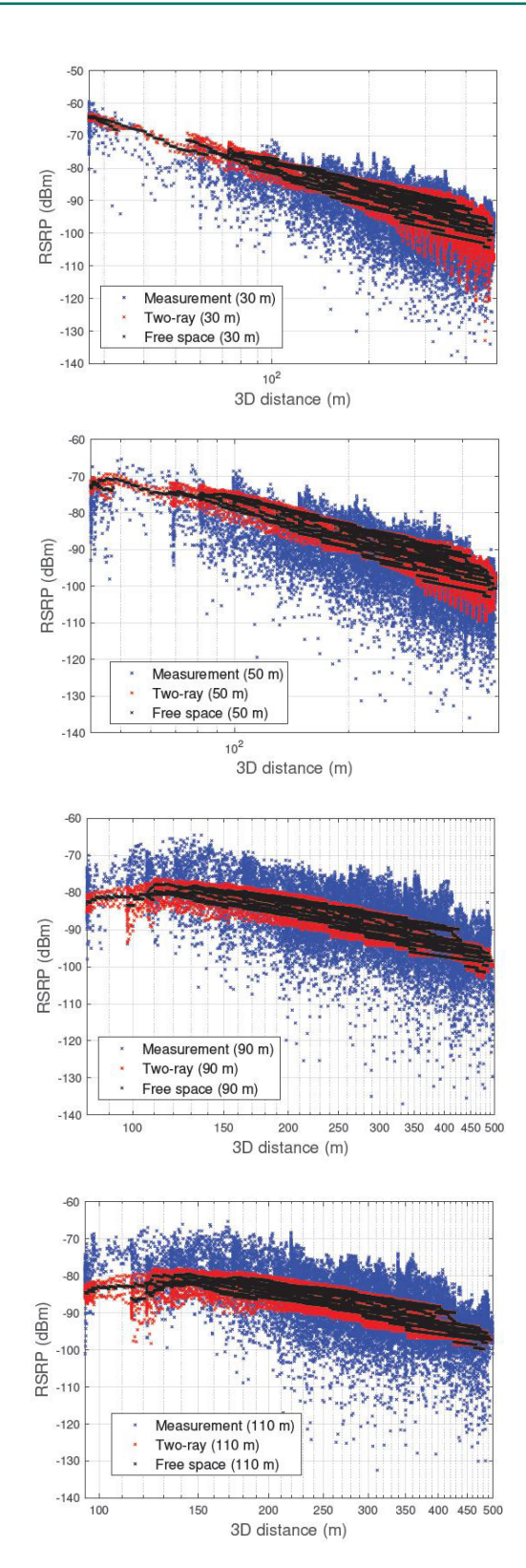


Fig. 10. Curve fitting for the RSRP measurements at different altitudes, considering free-space path loss and two-ray (ground-reflection) model.

C. Path Loss Model Fitting With Measurement

Fig. 10 illustrates the measured and fit RSRP values as a function of 3-D distance for different UAV heights ranging from 30 to 110 m. We adopt measured antenna patterns in Section IV-C. The fit curves follow the measured RSRP values

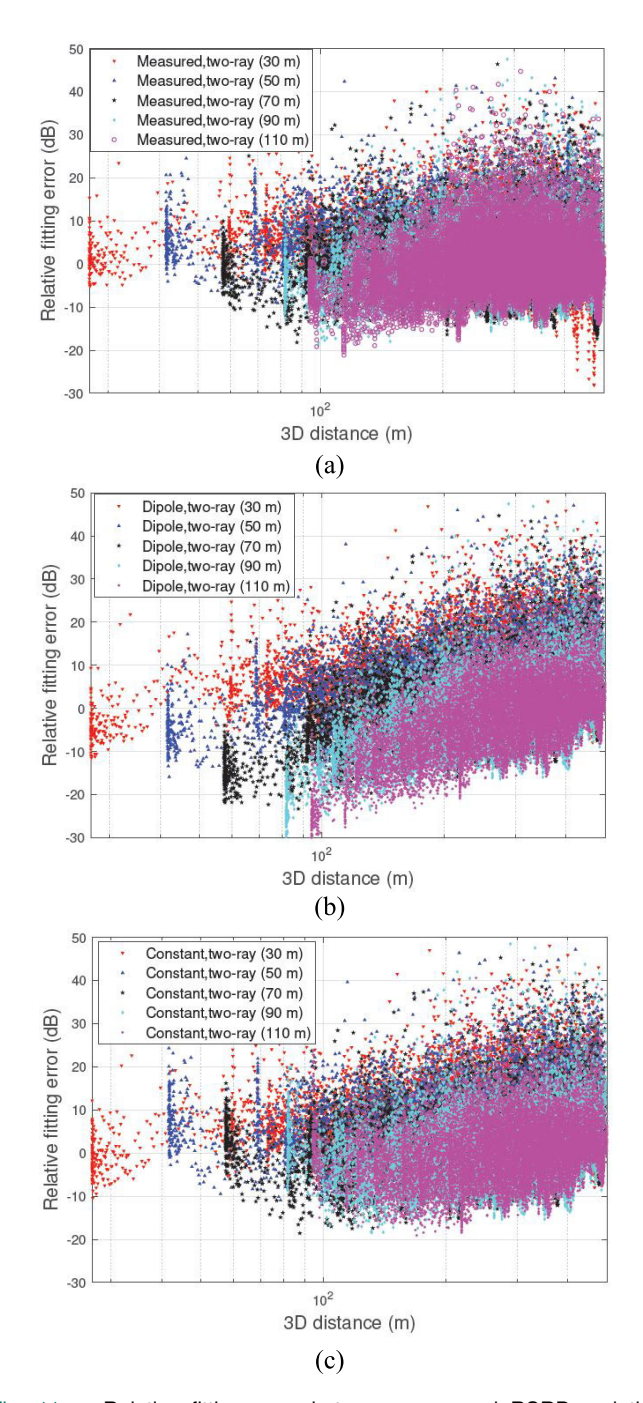


Fig. 11. Relative fitting error between measured RSRP and the two-ray path loss model with different antenna patterns and heights in distance domains. (a) Fitting error versus 3-D distance (measured antenna pattern). (b) Fitting error versus 3-D distance (dipole antenna pattern). (c) Fitting error versus 3-D distance (constant antenna pattern).

reasonably closely. It is worth noting that the two-ray path loss model performs better in capturing the fluctuation of signal strength due to the ground reflected path compared to the free-space path loss model, especially when the UAV height is low. In the logarithmic scale of the distance domain, the RSRP is expected to decrease linearly. However, in the short distance range, a concave curve can be observed. This phenomenon is a result of the elevation-dependent antenna gain and the dramatic change in the elevation angle at short

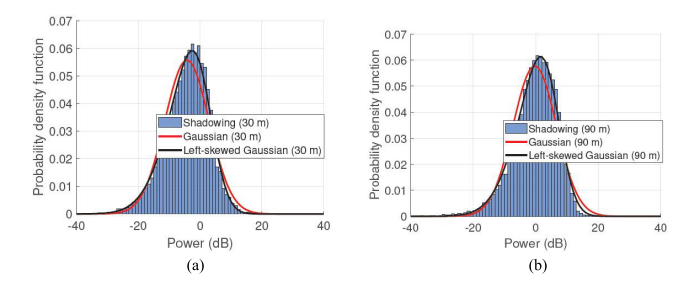


Fig. 12. Shadowing component from measurements and fit curves to Gaussian and skewed Gaussian distribution, at (a) 30 and (b) 90 m UAV altitude.

distances and high UAV altitudes. The 3-D antenna pattern considered in the path loss models effectively captures this effect, leading to more accurate RSRP fitting. Overall, the results in Fig. 10 highlight the importance of considering the elevation-dependent antenna gain and the 3-D antenna pattern in accurately modeling and fitting RSRP measurements in air-to-ground communications.

Fig. 11 shows the relative fitting error in the distance domain for all heights with different antenna patterns. The error by the dipole antenna pattern is relatively higher than other antenna patterns, especially when the distance is around 100–200 m due to the antenna pattern mismatch. We also observe that the fitting error for the omnidirectional antenna pattern is higher than the measured antenna pattern for a large distance. Overall, the use of the measured antenna pattern results in the best fit for the measured data.

D. Analysis of Shadowing Components From Measurement

After we derive the two-ray path loss model, we can extract the shadowing component by subtracting the path loss model from measured RSRP using (9), as shown in Fig. 12. The shadowing component is known to follow a Gaussian distribution, and the measured shadowing distributions for different UAV heights are compared to the fit curves. It is observed that the measured shadowing distributions can be modeled using a Gaussian distribution, though there are slight deviations. In particular, the measured distributions exhibit asymmetry with a heavier left tail compared to the symmetric Gaussian distribution. To achieve a better fit, an alternative approach is to use a skewed Gaussian (normal) distribution, which allows for introducing a desired level of skewness to the distribution [29]. The probability density function (pdf) of the skewed Gaussian distribution can be expressed as

$$f(x) = 2\phi \left(\frac{x - \xi}{\omega}\right) \Phi \left(\alpha \left(\frac{x - \xi}{\omega}\right)\right) \tag{21}$$

where $\phi(\cdot)$, $\Phi(\cdot)$ indicates the pdf and the cdf of Gaussian distribution, respectively. The parameter α in (21) decides the skewness of the distribution. If α is a positive real value, it gives right-skewness, while left-skewness is introduced by a negative real value. In addition, the mean, the standard deviation of the shadowing, left-skewed Gaussian parameter α , and normalized mean-squared error (NMSE) of model fittings for all heights are listed in Table II. Note that the optimal α is

TABLE II

MEAN AND STANDARD DEVIATION OF THE SHADOWING COMPONENT
FOR BOTH MEASUREMENT AND GAUSSIAN FITTING CURVE,
AND NMSE OF MODELS FITTING

| UAV height | Mean | Standard deviation | α | NMSE (Gaussian) | NMSE (skewed) |
|---------------|-----------|--------------------|-------|--------------------|------------------|
| 30 m | -4.26 dB | 7.14 dB | -2.13 | 0.0314 | 0.0027 |
| 50 m | -4.57 dB | 6.45 dB | -2.26 | 0.0370 | 0.0020 |
| 70 m | -0.34 dB | 6.53 dB | -2.57 | 0.0437 | 0.0036 |
| 90 m | -0.32 dB | 6.90 dB | -2.08 | 0.0338 | 0.0028 |
| _110 m | -0.27 dB | 6.83 dB | -2.27 | 0.0302 | 0.0022 |

decided by minimizing NMSE. It shows that the distributions and the value of variances in different heights are similar, and we can assume a stationary process in spatial data.

VI. NUMERICAL RESULTS ON 3-D SIGNAL INTERPOLATION

In this section, we will first study the horizontal, vertical, and finally 3-D correlation in the measured data. We will use the 3-D correlation to calculate the semi-variogram, which will subsequently be used to analyze the 3-D interpolation accuracy for various scenarios.

A. Analysis of Correlation Function From Measurement

1) Horizontal Distance Correlation: In this section, we analyze the spatial correlation using the AERPAW datasets available at [1]. We obtain correlation functions between two different 3-D locations by using measurements at different heights, and we use exponential and biexponential functions to model the correlations as discussed earlier. The mean and standard deviation values are obtained by statistical analysis in Section V-D and the measured RSRP values are utilized in calculating the correlations. We analyze the spatial correlation depending on the horizontal distance (d_h) with a zero vertical distance (d_v) by using the experiment dataset. Since our experiments fix the height of the drone for a specific flight, the vertical distance between the samples in the same flight is zero. The analysis of the correlation by the horizontal distance is performed by the following steps.

- Calculate the correlation among all samples in a flight, excluding the samples during the take-off and landing periods.
- 2) Sort the correlation from step 1) according to the horizontal distance between the sample pairs. This will ensure that the correlations are arranged in increasing order based on the horizontal distance.
- 3) Average the correlations every 2 m. Start from the smallest horizontal distance and group the correlations within a 2-m interval. Calculate the average correlation for each interval. Repeat this process for subsequent 2 m intervals until covering all the correlations.
- 4) Perform steps 1)–3) iteratively for each height (30, 50, 70, 90, and 110 m). Then, we have correlations for each individual height.
- 5) Average the correlation for every distance over all the heights. Take the correlations obtained in step 4) for each

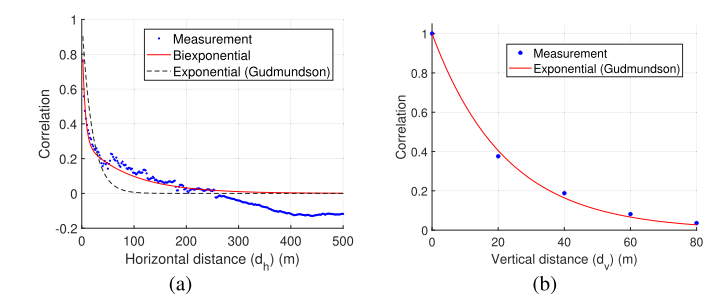


Fig. 13. Correlation of RSRP measurements with horizontal and vertical distances and curve fits with exponential and biexpontential models. (a) Correlation of horizontal distance. (b) Correlation of vertical distance.

height and distance, and compute the average correlation value across all heights for that specific distance.

The correlation between two samples w_i and w_j is calculated by

$$R_{i,j} = \frac{(w_i - v_i)(w_j - v_j)}{\sigma_{w,i}\sigma_{w,j}}$$
 (22)

where ν and σ_w denote the mean and the standard deviation of the sample, which can be obtained from Table II. The obtained correlation function and fit curves are shown in Fig. 13(a). It is observed that the correlation is rapidly decayed as the horizontal distance increases. Although the correlation is generally modeled by an exponential function (also known as the Gudmundson model) [11], the biexponential model [30] fits better than the exponential model for our measurements, which is given as

$$R(d_{\rm h}) = ae^{-b_1d_{\rm h}} + (1-a)e^{-b_2d_{\rm h}}$$
 (23)

where b_1 and b_2 are fitting parameters. We also observe that the correlation distance is 4.5 m when the correlation is 0.5.

2) Vertical Distance Correlation: We calculate the vertical distance correlation with a zero horizontal distance from measurements which is opposite to Section VI-A1. Since the trajectory of the UAV for flights at different heights is designed to be identical (see Fig. 5), we can obtain samples of the same 2-D location (latitude, longitude) with different vertical distances. For example, if we want to obtain 20 m vertical distance samples, we can use the dataset from the 30- and 50-m UAV flights and pick two samples from any overlapped trajectory (one from the 30-m height, the other from the 50-m height). The analysis of the correlation by the vertical distance is conducted by the following steps.

- 1) Choose two different height measurements datasets, such as the datasets from the 30- and 50-m UAV flights.
- 2) Remove data where the two trajectories are not fully overlapped, using a threshold of $d_h > 3$ m. This ensures that we have data points with the same location across the trajectories.
- 3) Calculate the correlations between the two samples with the same location across the trajectories. Compute the correlation coefficient for each pair of samples and average them out. This will give you the correlation for a specific vertical distance (e.g., 20 m) between the two heights.

TABLE III
CORRELATIONS BETWEEN DIFFERENT UAV HEIGHTS

| | 30 m | 50 m | 70 m | 90 m | 110 m |
|-------|--------|--------|-------|--------|--------|
| 30 m | 1.003 | 0.247 | 0.080 | -0.024 | -0.040 |
| 50 m | 0.247 | 1.004 | 0.214 | 0.057 | -0.002 |
| 70 m | 0.080 | 0.214 | 1.003 | 0.307 | 0.172 |
| 90 m | -0.024 | 0.057 | 0.307 | 1.001 | 0.409 |
| 110 m | -0.040 | -0.002 | 0.172 | 0.409 | 1.012 |

4) Repeat steps 1) to 3) iteratively for pairs of measurements at different heights. For example, we can calculate correlations for the 50- and 70-m flights, 70- and 90-m flights, and so on.

In step 2), we exclude the samples that the trajectory is undesirably not overlapped by checking GPS readings. The correlations between different pairs of flights are listed in Table III. We also present the obtained correlation function from Table III and the fit curve in Fig. 13(b). It is observed that the correlation function based on the vertical distance fits best with the exponential model, which is expressed as

$$R(d_{\mathbf{v}}) = e^{-\frac{d_{\mathbf{v}}}{d_{\mathbf{cor}}} \ln(2)} \tag{24}$$

where the correlation distance is given by $d_{cor} = 11.24$ m.

- 3) 3-D Distance Correlation: To analyze the correlation when both horizontal distance and vertical distance are considered, we can process the dataset obtained from flights at two different heights. By comparing the measurements from these flights, you can determine the correlation between two different 3-D coordinate locations. The processing steps for obtaining correlation with 20 m vertical distance are as follows.
 - 1) Choose a pair of measurement datasets where the height difference is 20 m. For example, select the dataset from the 30-m height flight and the dataset from the 50-m height flight.
 - 2) Calculate the correlation between a sample from one height (e.g., 30 m) and a sample from the other height (e.g., 50 m) across all the samples in the datasets.
 - Sort the correlation from step 2) by the horizontal distance and average the correlations for every 2 m of horizontal distance.
 - 4) Repeat steps 1) to step 3) iteratively by different pairs of the measurement datasets of the height. For example, you can repeat the analysis with the dataset from the 50-m height flight and the dataset from the 70-m height flight.

By performing this iterative analysis for different pairs of measurement datasets with varying height differences, we can obtain the correlation values that capture the relationship between joint horizontal and vertical distances. This analysis helps in understanding how the signal strength correlation varies with changes in both horizontal and vertical distances, providing insights into the spatial characteristics of the wireless channel.

The 3-D distance correlation results with 20 and 40 m vertical distances are shown in Fig. 14. We model and fit

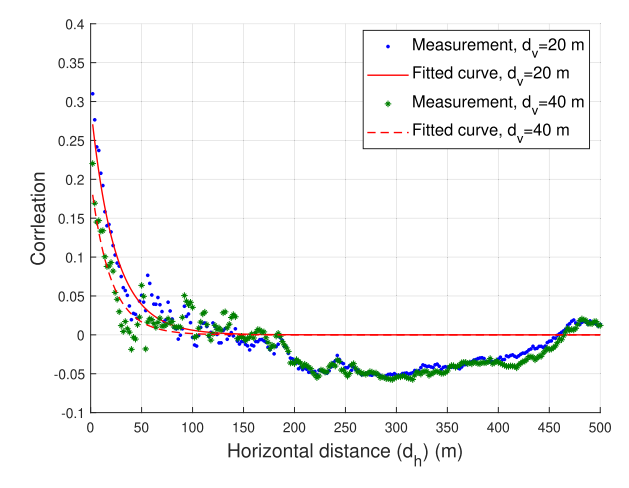


Fig. 14. 3-D distance correlation and fit curve by the proposed model where vertical distance (d_V) = 20, 40 m.

TABLE IV FITTING PARAMETERS b_1 , b_2 IN (25) DEPENDING ON THE VERTICAL DISTANCE

| $d_{ m v}$ | b_1 | b_2 |
|------------|---------|---------|
| 0 m | 0.02815 | 0.2474 |
| 20 m | 0.05988 | 0.03574 |
| 40 m | 0.06998 | 0.045 |

the correlation of joint horizontal and vertical distance by combining the correlation functions of the horizontal and the vertical distance in (23) and (24). The proposed correlation model in 3-D space is expressed as

$$R(d_{\rm v}, d_{\rm h}) = e^{-\frac{d_{\rm v}}{d_{\rm cor}} \ln(2)} \left(a e^{-b_1 d_{\rm h}} + (1 - a) e^{-b_2 d_{\rm h}} \right) \tag{25}$$

where a=0.3, and b_1 , b_2 are tuning parameters. Note that when $d_h=0$, the model is the same as (23), while when $d_v=0$, the model is equivalent to (24). The fit values of b_1 , b_2 depending on the vertical distance (d_v) are listed in Table IV.

B. Analysis of Semi-Variogram

In Section III-A, we introduce earlier the concept of semi-variogram in (11) and derive the relation to the correlation function in (12). We analyze the semi-variogram by measurements results in Fig. 15 with respect to both the horizontal distance and vertical distance. The measurement results are directly obtained by the definition of the semi-variogram in (11) and the analysis results come from the correlation function in (25) which is then used in (12). The measurements and our analysis from (12) are closely overlapped for both distance conditions.

C. Performance Evaluation With Kriging

In this section, we evaluate the 3-D interpolation performance of the Kriging technique described in Section III-B using the measurement dataset. We adopt cross-validation-based RMSE evaluation [15], which compares the predicted RSRP with the measured RSRP to observe the error. In particular, the RMSE for performance evaluation can be expressed

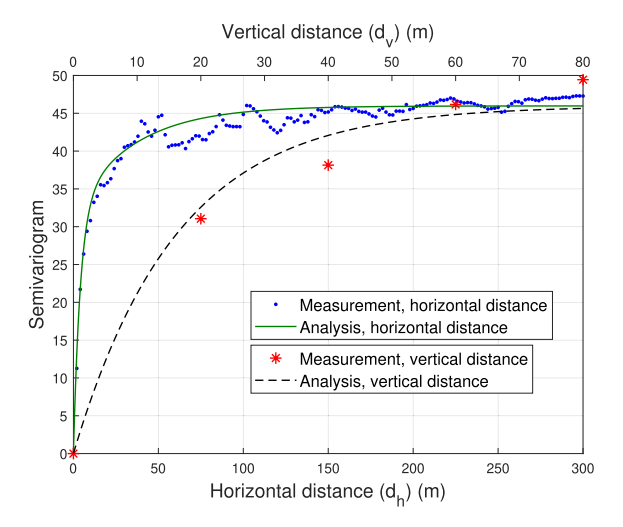


Fig. 15. Measured semi-variogram and analysis by the correlation functions in (23) and (24), with respect to horizontal distance (bottom x-axis), and vertical distance (top x-axis).

as

RMSE =
$$\sqrt{\frac{1}{N_0} \sum_{i}^{N_0} \left(\hat{r}(l_{0,i}^{\text{uav}}) - r(l_{0,i}^{\text{uav}}) \right)^2}$$
 (26)

where N_0 denotes the number of samples for prediction. In our evaluation, the 30-m height measurement samples are predicted by 30, 50, and 70 m height measurement datasets. The cross-validation-based evaluation is conducted by the following steps.

- 1) Randomly select *M* samples from the measurement dataset to use for the prediction. These samples will serve as the training set.
- 2) Randomly select N_0 samples from the 30-m measurement dataset as the validation set for cross-validation.
- 3) Use the Kriging technique described in Section III-B to predict the RSRP values for the N_0 validation samples based on the M training samples.
- 4) Calculate RMSE between the predicted RSRP values and the actual measured RSRP values for the N_0 validation samples. The RMSE is calculated using (26).
- 5) Repeat steps 1) to 4) iteratively for a large number of times, such as 10 000 iterations and calculate the median for the RMSE values obtained from the iterations. The median value represents the overall prediction performance of the Kriging technique.

In step 2), after randomly selecting M samples for prediction, exclude those samples from the dataset chosen for cross-validation. This ensures that the samples used for prediction are not used for validation. In addition, when we predict a sample by Kriging in step 3), when predicting a sample using Kriging, consider only the nearby samples within a certain distance threshold (r_0) . Limit the selection of neighboring samples to those within the r_0 radius circle around the target sample. These nearby samples will be used to predict the RSRP value for the target sample. The snapshot of the randomly chosen M samples from 50 m height measurement

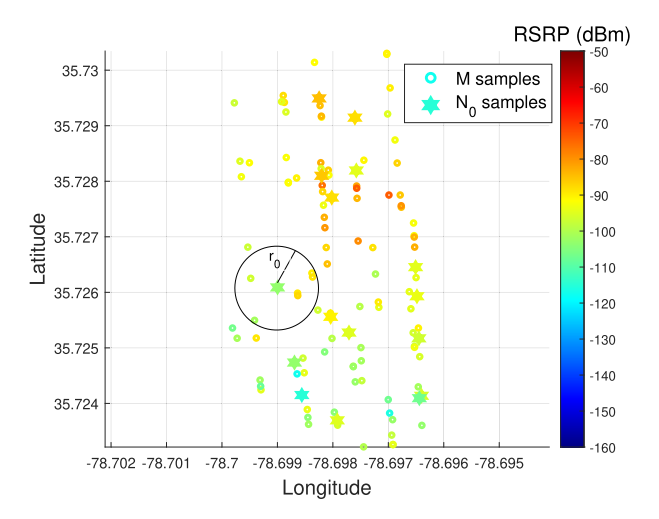


Fig. 16. Snapshot of the randomly chosen samples for Kriging.

and N_0 from 30 m height measurement is described in Fig. 16. The figure depicts the radius circle r_0 within which nearby samples are used to predict the target sample. To provide a benchmark for comparison, we consider the perfect path loss-based 3-D interpolation. In particular, we assume that the BS has perfect knowledge of the exact path loss and transmit power for all locations. This represents the ideal condition for prediction without utilizing spatial correlation. The RMSE by the perfect path loss estimation is equivalent to the standard deviation of the shadowing component from (9) and (26) as follows:

$$\mathsf{RMSE}_{\mathsf{ple}} = \sqrt{\mathbb{E}\left[\left(\hat{r} - r\right)^{2}\right]} = \sqrt{\mathbb{E}\left[w^{2}\right]} = \sigma_{w}. \tag{27}$$

In Fig. 17, the RMSE performance of Kriging using measurements at different UAV altitudes is presented. The results show that the performance of Kriging varies depending on the altitude of the measurements used for prediction. When utilizing the 30- and 50-m height measurement data for prediction, Kriging outperforms the perfect path loss estimation. This indicates that Kriging can leverage the spatial correlation present in the highly corrected data to achieve better prediction accuracy. However, in the case of 70 m height measurement, the perfect path loss estimation performs better than Kriging. This suggests that the correlation at a vertical distance of 60 m is too low to accurately predict using Kriging.

In Fig. 17(a), it is observed that the RMSE generally decreases as the number of samples used for prediction (N) increases. However, when N exceeds 250, the performance of Kriging with an r_0 value of 200 m is the worst among the three different r_0 values considered. This indicates that while a larger number of samples can improve performance, adding low-correlated samples can degrade the prediction accuracy. It is important to strike a balance and choose an appropriate number of samples (M) and radius (r_0) .

Furthermore, in Fig. 17(b), the RMSE initially decreases and then increases for r_0 values of 70, 100, and 200 m. This suggests that if the correlation between samples is not sufficiently high, increasing the number of samples may not

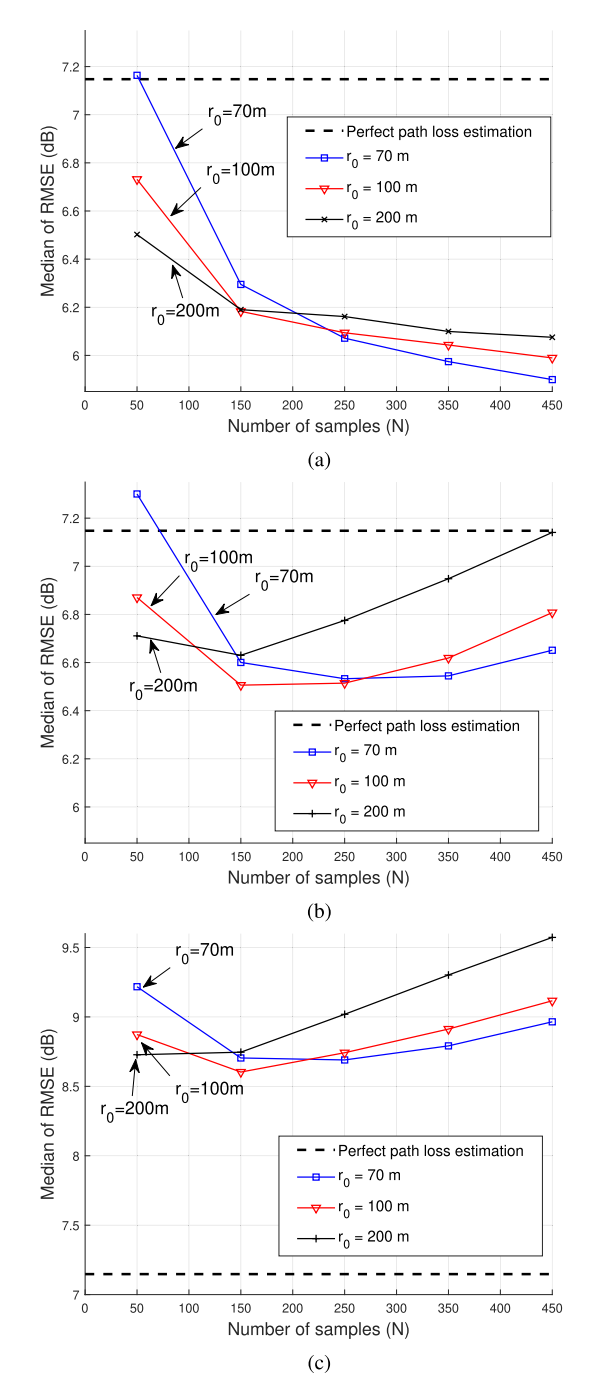


Fig. 17. RMSE of the prediction at 30 m UAV altitude from measurements at 30, 50, and 70 m UAV heights by Kriging, which is benchmarked by the perfect path loss estimation. (a) Prediction by 30 m height measurement. (b) Prediction by 50 m height measurement. (c) Prediction by 70 m height measurement.

necessarily lead to improved performance. It highlights the importance of considering both the number of samples and the correlation when determining the optimal parameters for Kriging prediction.

In conclusion, the choice of the number of samples (M) and radius (r_0) is crucial for achieving accurate predictions using Kriging. Utilizing a larger number of highly correlated samples can improve performance, while including low-correlated samples or selecting an inappropriate radius can degrade the prediction accuracy.

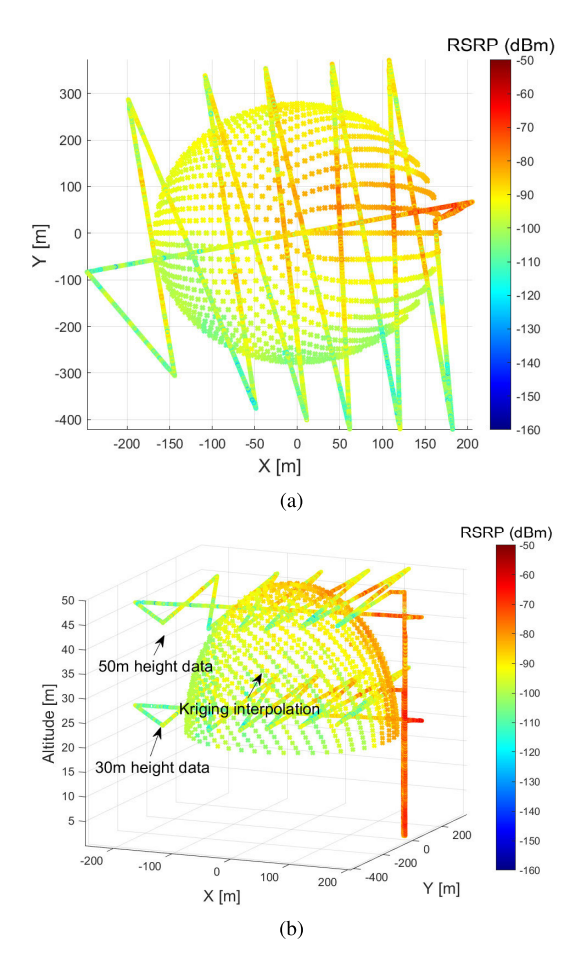


Fig. 18. 3-D radio map from Kriging interpolation using the measurements at 30 and 50 m UAV altitudes. (a) Top view. (b) 3-D view.

D. 3-D Interpolation by Kriging

Fig. 18 displays the generated 3-D radio map of RSRP using the Kriging interpolation technique with the available measurement data at 30 and 50 m heights. The map provides a visual representation of the RSRP distribution in the 3-D space. The dome shape of the 3-D radio map provides valuable insights into monitoring the signal leakage in the 3-D volume of the RDZ. By examining the map, one can observe the spatial variations and signal strength levels within the monitored area. The dense 3-D radio map obtained through Kriging interpolation enables efficient analysis and decision-making related to signal monitoring, interference management, and overall RF planning within the monitored area. In particular, a spectrum monitoring engine (SME) can estimate the received signal strength from each signal served within the RDZ on the surface of the dome. Subsequently, interference to sensitive receivers outside of the RDZ can be extrapolated, and if exceed a threshold, interfering signal services in the RDZ can take action (e.g., rescheduling to a different band or reducing power).

VII. CONCLUSION

In this article, we introduce the RDZ concept which efficiently manages and controls the spectrum usage by monitoring the signal occupancy and leakage in a real-time fashion. To monitor the signal leakage from an area, we need to develop a radio map of signal power surrounding the area, which is

more challenging when considering a 3-D space. We propose a signal power interpolation method in the 3-D volume that uses Kriging. The correlation model between two different 3-D locations is designed and the semi-variogram is defined and analyzed. In addition, we study the proposed 3-D Kriging interpolation using an experimental dataset provided by the NSF AERPAW platform. We fit path loss and shadowing models to the RSRP measurements and study the performance of the Kriging interpolation technique for various scenarios. Our results show that significant gains are possible in received power estimation accuracy by utilizing the 3-D correlation of the data when compared with using only a path loss-based power estimation.

ACKNOWLEDGMENT

The authors would like to thank NSF's associated supplement for studying National Radio Dynamic Zones (NRDZs). They would also like to thank Wireless Research Center for measuring antenna patterns by using an anechoic chamber. The datasets and post-processing scripts for obtaining the results in this manuscript are publicly accessible at [1].

REFERENCES

- [1] S. J. Maeng, O. Ozdemir, I. Guvenc, M. Sichitiu, and R. Dutta. (2022). LTE I/Q Measurement By AERPAW Platform for Air-to-Ground Propagation Modeling. IEEE Dataport. [Online]. Available: https://dx.doi.org/10.21227/0p43-0d72
- [2] M. Zheleva, C. R. Anderson, M. Aksoy, J. T. Johnson, H. Affinnih, and C. G. DePree, "Radio dynamic zones: Motivations, challenges, and opportunities to catalyze spectrum coexistence," *IEEE Commun. Mag.*, vol. 61, no. 6, pp. 156–162, Jan. 2023.
- [3] S. J. Maeng et al., "National radio dynamic zone concept with autonomous aerial and ground spectrum sensors," in *Proc. IEEE Int.* Conf. Commun. Workshops (ICC Workshops), May 2022, pp. 687–692.
- [4] S. Tschimben et al., "Testbed for radio astronomy interference characterization and spectrum sharing research," in *Proc. IEEE Aerosp. Conf.*, Farah, MT, USA, Mar. 2023, pp. 1–16.
- [5] NSF Program Solicitation. (Jun. 2022). Spectrum Innovation Initiative: National Radio Dynamic Zones (SII-NRDZ). [Online]. Available: https://www.nsf.gov/pubs/2022/nsf22579/nsf22579.htm
- [6] H. Zou, M. Jin, H. Jiang, L. Xie, and C. J. Spanos, "WinIPS: WiFibased non-intrusive indoor positioning system with online radio map construction and adaptation," *IEEE Trans. Wireless Commun.*, vol. 16, no. 12, pp. 8118–8130, Dec. 2017.
- [7] A. Ivanov, B. Muhammad, K. Tonchev, A. Mihovska, and V. Poulkov, "UAV-based volumetric measurements toward radio environment map construction and analysis," *Sensors*, vol. 22, no. 24, p. 9705, Dec. 2022.
- [8] H. B. Yilmaz, T. Tugcu, F. Alagöz, and S. Bayhan, "Radio environment map as enabler for practical cognitive radio networks," *IEEE Commun. Mag.*, vol. 51, no. 12, pp. 162–169, Dec. 2013.
- [9] F. Graziosi and F. Santucci, "A general correlation model for shadow fading in mobile radio systems," *IEEE Commun. Lett.*, vol. 6, no. 3, pp. 102–104, Mar. 2002.
- [10] S. S. Szyszkowicz, H. Yanikomeroglu, and J. S. Thompson, "On the feasibility of wireless shadowing correlation models," *IEEE Trans. Veh. Technol.*, vol. 59, no. 9, pp. 4222–4236, Nov. 2010.

- [11] M. Gudmundson, "Correlation model for shadow fading in mobile radio systems," *Electron. Lett.*, vol. 27, no. 23, p. 2145, 1991.
- [12] R. He, Z. Zhong, B. Ai, and C. Oestges, "Shadow fading correlation in high-speed railway environments," *IEEE Trans. Veh. Technol.*, vol. 64, no. 7, pp. 2762–2772, Jul. 2015.
- [13] H. Braham, S. B. Jemaa, G. Fort, E. Moulines, and B. Sayrac, "Fixed rank Kriging for cellular coverage analysis," *IEEE Trans. Veh. Technol.*, vol. 66, no. 5, pp. 4212–4222, May 2017.
- [14] K. Sato and T. Fujii, "Kriging-based interference power constraint: Integrated design of the radio environment map and transmission power," *IEEE Trans. Cognit. Commun. Netw.*, vol. 3, no. 1, pp. 13–25, Mar. 2017.
- [15] K. Sato, K. Suto, K. Inage, K. Adachi, and T. Fujii, "Space-frequency-interpolated radio map," *IEEE Trans. Veh. Technol.*, vol. 70, no. 1, pp. 714–725, Jan. 2021.
- [16] Z. Wei, R. Yao, J. Kang, X. Chen, and H. Wu, "Three-dimensional spectrum occupancy measurement using UAV: Performance analysis and algorithm design," *IEEE Sensors J.*, vol. 22, no. 9, pp. 9146–9157, May 2022.
- [17] A. Al-Hourani and K. Gomez, "Modeling cellular-to-UAV path-loss for suburban environments," *IEEE Wireless Commun. Lett.*, vol. 7, no. 1, pp. 82–85, Feb. 2018.
- [18] J. Holis and P. Pechac, "Elevation dependent shadowing model for mobile communications via high altitude platforms in built-up areas," *IEEE Trans. Antennas Propag.*, vol. 56, no. 4, pp. 1078–1084, Apr. 2008.
- [19] M. Simunek, F. P. Fontán, and P. Pechac, "The UAV low elevation propagation channel in urban areas: Statistical analysis and timeseries generator," *IEEE Trans. Antennas Propag.*, vol. 61, no. 7, pp. 3850–3858, Jul. 2013.
- [20] S. J. Maeng, İ. Güvenç, M. L. Sichitiu, and O. Ozdemir, "Out-of-zone signal leakage sensing in radio dynamic zones," in *Proc. IEEE Int. Conf. Commun. (ICC)*, May 2022, pp. 5579–5584.
- [21] T. Kidd. (Jun. 2018). CHIPS—The Department of Navy's Information Technology Magazine. National Radio Quiet and Dynamic Zones. [Online]. Available: https://www.doncio.navy.mil/CHIPS/ArticleDetails. aspx?ID=10299
- [22] N. R. Chopde and M. Nichat, "Landmark based shortest path detection by using A* and Haversine formula," *Int. J. Innov. Res. Comput. Commun. Eng.*, vol. 1, no. 2, pp. 298–302, Apr. 2013.
- [23] W. C. Jakes and D. C. Cox, *Microwave Mobile Communications*. Hoboken, NJ, USA: Wiley-IEEE Press, 1994.
- [24] N. Cressie, *Statistics for Spatial Data*. Hoboken, NJ, USA: Wiley, 2015.
- [25] Octane Wireless. SA-1400-5900 Data Sheet. Accessed: Sep. 2019. [Online]. Available: https://www.octanewireless.com/product/sa-1400-5900-tri-band-stub-antenna/
- [26] Mobile Mark Inc. RM-WB1 Series Radiation Pattern. Accessed: May 2020. [Online]. Available: https://www.mobilemark.com/product/ rm-wb1/
- [27] S. J. Maeng, O. Ozdemir, I. Güvenç, M. L. Sichitiu, R. Dutta, and M. Mushi, "AERIQ: SDR-based LTE I/Q measurement and analysis framework for air-to-ground propagation modeling," in *Proc. IEEE Aerosp. Conf.*, Big Sky, MT, USA, Mar. 2023, pp. 1–11.
- [28] S. J. Maeng, M. A. Deshmukh, I. Güvenç, A. Bhuyan, and H. Dai, "Interference analysis and mitigation for aerial IoT considering 3D antenna patterns," *IEEE Trans. Veh. Technol.*, vol. 70, no. 1, pp. 490–503, Jan. 2021.
- [29] C. K. Sung, S. Li, M. Hedley, N. Nikolic, and W. Ni, "Skew log-normal channel model for indoor cooperative localization," in *Proc. IEEE 28th Annu. Int. Symp. Pers., Indoor, Mobile Radio Commun. (PIMRC)*, Montreal, QC, Canada, Oct. 2017, pp. 1–5.
- [30] L. Liu, C. Tao, D. W. Matolak, T. Zhou, and H. Chen, "Investigation of shadowing effects in typical propagation scenarios for high-speed railway at 2350 MHz," *Int. J. Antennas Propag.*, vol. 2016, pp. 1–8, 2016.